CMS Physics Analysis Summary

Contact: cms-pag-conveners-higgs@cern.ch 2022/08/12

Search for a new resonance decaying to two scalars in the final state with two bottom quarks and two photons in proton-proton collisions at $\sqrt{s} = 13\,\text{TeV}$

The CMS Collaboration

Abstract

A search for new resonances in the final state with two bottom quarks and two photons is presented, using CERN LHC proton-proton collision data collected by the CMS experiment at $\sqrt{s} = 13$ TeV, and corresponding to an integrated luminosity of 138 fb^{-1}. The resonance X decays into either a pair of the standard model Higgs bosons HH, or an H and a new scalar Y having a mass $m_\text{Y} < m_\text{X} - m_\text{H}$. A model-independent analysis is performed with a narrow-width approximation for X in the mass range 260 GeV $-$ 1 TeV (for the HH decay) and 300 GeV $-$ 1 TeV (for the HY decay), covering a mass range of $90 < m_\text{Y} < 800$ GeV. The upper limits at 95% confidence level on the product of the production cross section of spin-0 X and its decay branching fraction to HH are observed to be within $0.82 - 0.07$ fb, while the corresponding expected limits are $0.74 - 0.08$ fb, depending upon the considered mass range in m_X. For the X decaying to HY, the observed limits lie in the range $0.90 - 0.04$ fb whereas the expected limits are $0.79 - 0.05$ fb, with the considered mass ranges in m_X and m_Y. The largest deviation from background-only hypothesis with local (global) significance of 3.8 (2.8) standard deviations is observed for $m_\text{X} = 650$ GeV and $m_\text{Y} = 90$ GeV. The HH limits are compared with predictions in the warped extra dimensional model. The HY limits are interpreted with the next-to-minimal supersymmetric standard model and the two-real-scalar-singlet model.

This document has been revised with respect to the version dated July 8th, 2022.

1 Introduction

Since the discovery of a Higgs boson H in 2012 at the CERN LHC by the ATLAS and CMS Collaborations [1–3], the standard model of particle physics (SM) has been validated as the most promising theory to understand the interactions of elementary particles [4–8]. With the measurement of the Higgs boson mass of 125.38 GeV [9], all the SM parameters are now established. Despite its success, the SM still has shortcomings in explaining many observed phenomena such as dark matter, gravity and baryogenesis. Therefore, beyond the standard model (BSM) theories have been postulated, which address these open questions and which are being explored at the LHC.

Among the BSM theories, models with warped extra dimensions (WEDs) [10] predict the existence of small and compactified extra dimensions along which gravity particles propagate. In the "Randall-Sundram (RS) bulk model", matter particles are also allowed to propagate along the extra dimensions. The model explains the nature of gravitational forces and provides a solution to the SM hierarchy problem. This model contains resonance particles, the spin-0 radion [11–13] and the spin-2 first Kaluza-Klein (KK) excitation of the graviton [14–16], which have sizeable branching fractions in decaying to Higgs boson pairs HH.

The supersymmetric theory (SUSY) is an extension to the SM that postulates a symmetry pairing fermions with bosons and vice-versa (superpartners) [17, 18]. The minimal supersymmetric standard model (MSSM) extends the SM Lagrangian by introducing another complex Higgs doublet [19, 20]. The next-to-minimal supersymmetric standard model (NMSSM) [21, 22] introduces one additional complex singlet field to MSSM. The NMSSM is the most straightforward supersymmetric extension to the SM where the electroweak scale originates from the SUSY-breaking scale. Hence it provides a solution to the well-known MSSM μ problem [23]. In the NMSSM scenario, several scalar particles emerge, one of which can be associated with the 125 GeV Higgs boson discovered so far. The more massive Higgs bosons may decay to lighter Higgs bosons in this model.

Apart from the NMSSM, the searches are also motivated from the two-real-scalar-singlet model (TRSM) [24]. The TRSM is an extension of the SM where two additional singlet fields are added. The mixing between the Higgs scalar field and these additional scalar fields gives three massive scalars among which one scalar field is identified as SM-like Higgs boson. The heaviest scalar is allowed to decay into lighter scalars giving the same topology as the Higgs-to-Higgs decay process.

This note presents the results of searches for a massive particle X decaying either to HH or to H and a new lighter scalar Y, using LHC proton-proton (pp) collision data collected by the CMS experiment in 2016–2018 at $\sqrt{s} = 13$ TeV and amounting to a total integrated luminosity of 138 fb^{-1}. The searches do not assume X and Y to belong to any specific BSM theory. However, the process $\text{pp} \to \text{X} \to \text{HH}$ may be interpreted as the production and subsequent decay of a bulk graviton or a bulk radion in the RS bulk model. Similarly, in the process $\text{pp} \to \text{X} \to \text{HY}$, the X can be interpreted as a heavy scalar which decays to a lighter scalar Y and a Higgs boson according to NMSSM.

The searches are performed in the $\gamma\gamma\text{b}\bar{\text{b}}$ final state. Figure 1 shows the Feynman diagram of the signal process. With this channel, the analysis benefits from the combination of the $\text{H} \to \gamma\gamma$ decay, with its large signal purity, and the $\text{H} \to \text{b}\bar{\text{b}}$ or $\text{Y} \to \text{b}\bar{\text{b}}$ decay, which gives a large branching fraction. For the Higgs boson, the SM decay branching fractions are assumed.

The analysis uses a strategy similar to the search for nonresonant production of HH [25, 26]. One Higgs boson is reconstructed from a pair of photons $\gamma\gamma$ and their invariant mass $m_{\gamma\gamma}$ is

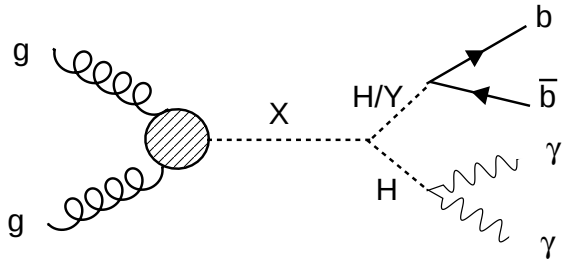

Figure 1: Feynman diagram showing gluon-gluon fusion production of a BSM resonance X decaying to a pair of scalars (HH or HY), which then decay to the $\gamma\gamma b\bar{b}$ final state.

required to be compatible with the Higgs boson mass. Two pairs of jets, identified as originating from b quarks, are paired to form the other Higgs boson or a new resonance Y of unknown mass. A simultaneous fit of $m_{\gamma\gamma}$ and the b jet pair invariant mass m_{jj} is used to extract the signal.

This note is organized as follows: Section 2 provides a brief description of the CMS detector followed by the details of the data and simulations in Section 3. The analysis strategy is discussed in Section 4 including background rejection methods with signal and background modeling studies. Section 5 details the systematic uncertainties. The results are presented in Section 6 and the analysis is summarized in Section 7.

2 The CMS detector

The central feature of the CMS apparatus is a superconducting solenoid of 6 m internal diameter, providing a magnetic field of 3.8 T. Within the solenoid volume, there is a silicon pixel and strip tracker, a lead tungstate crystal electromagnetic calorimeter (ECAL), and a brass and scintillator hadron calorimeter (HCAL), each composed of a barrel and two endcap sections. Forward calorimeters extend the pseudorapidity (η) coverage provided by the barrel and endcap detectors. Muons are detected in gas-ionization chambers embedded in the steel flux-return yoke outside the solenoid. A more detailed description of the CMS detector, together with a definition of the coordinate system and the relevant kinematic variables, can be found in Ref. [27].

Events of interest are selected using a two-tiered trigger system [28]. The first level (L1), composed of custom hardware processors, uses information from the calorimeters and muon detectors to select events at a rate of around 100 kHz within a time interval of less than 4 μs. The second level, known as the high-level trigger (HLT), consists of a farm of processors running a version of the full event reconstruction software optimized for fast processing, and reduces the event rate to around 1 kHz before data storage [29].

The particle-flow algorithm [30] (PF) aims to reconstruct and identify each individual particle in an event (PF candidate), with an optimized combination of information from the various elements of the CMS detector. The energy of photons is obtained from the ECAL measurement. The energy of electrons is determined from a combination of the track momentum at the main interaction vertex, the corresponding ECAL cluster energy, and the energy sum of all bremsstrahlung photons attached to the track. The momentum of muons is obtained from the curvature of the corresponding track. The energy of charged hadrons is determined from a combination of their momentum measured in the tracker and the matching ECAL and HCAL energy deposits, corrected for zero-suppression effects and for the response function of the calorimeters to hadronic showers. Finally, the energy of neutral hadrons is obtained from the

corresponding corrected ECAL and HCAL energies.

For each event, hadronic jets are clustered from these reconstructed particles using the infrared and collinear safe anti-k_T algorithm [31, 32] with a distance parameter of 0.4. Jet momentum is determined as the vectorial sum of all particle momenta in the jet, and is found from simulation to be, on average, within 5 to 10% of the true momentum over the whole transverse momentum (p_T) spectrum and detector acceptance. Additional pp interactions within the same or nearby bunch crossings can contribute additional tracks and calorimetric energy depositions, increasing the apparent jet momentum. To mitigate this effect, tracks identified to be originating from pileup vertices are discarded, and an offset correction is applied to correct for remaining contributions. Jet energy corrections are derived from simulation studies so that the average measured energy of jets becomes identical to that of particle-level jets. In situ measurements of the momentum balance in dijet, photon+jet, Z+jet, and multijet events are used to determine any residual differences between the jet energy scale in data and simulation, and appropriate corrections are made [33]. Additional selection criteria are applied to each jet to remove jets potentially dominated by instrumental effects or reconstruction failures. The jet energy resolution amounts typically to 15–20% at 30 GeV, 10% at 100 GeV, and 5% at 1 TeV [33].

The missing transverse momentum vector $\vec{p}_T^{\,\text{miss}}$ is computed as the negative vector sum of the transverse momenta of all the PF candidates in an event, and its magnitude is denoted as p_T^{miss} [34]. The $\vec{p}_T^{\,\text{miss}}$ is modified to account for corrections to the energy scale of the reconstructed jets in the event.

3 Data and simulation samples

The data used for the analysis were collected by the CMS detector from LHC pp collisions at $\sqrt{s} = 13$ TeV in 2016–2018. The total analyzed data have an integrated luminosity of 138 fb^{-1} [35–37]. Events are collected using a 2016 (2017 and 2018) trigger requiring two photons with momentum thresholds $p_T^{\gamma_1} > 30$ GeV and $p_T^{\gamma_2} > 18$ (22) GeV and having their invariant mass exceeding 90 GeV, where γ_1 and γ_2 represent leading and subleading photon, respectively. The photons in the trigger algorithm are also required to pass loose selections on their calorimeter shower shapes, on the ratio of their energies deposited in the HCAL to that in the ECAL (identification variable), and on the p_T carried by charged hadrons in the vicinity (isolation requirement) [38].

For the signal process, we study the resonant production from gluon-gluon fusion. Signal samples have been generated using MADGRAPH5_aMC@NLO, versions 2.2.2 (2016)/2.4.2 (2017, 2018) (for WED) and 2.6.5 (for NMSSM) [39, 40].

The dominant backgrounds include the SM nonresonant multijet processes with prompt photons, irreducible prompt diphoton production ($\gamma\gamma$ + jets), and the reducible background from γ + jets events. The nonresonant background simulations are used only in the multivariate discriminant, optimization, and validation studies of the analysis. A data-driven method is used for background estimation. The $\gamma\gamma$ + jets background is modeled with SHERPA v.2.2.1 [41] at leading order (LO) and includes up to three additional partons at the matrix element level. The γ + jets background is modeled with PYTHIA 8.212 [42] at LO.

Single Higgs boson production, where the Higgs boson decays to a pair of photons, is considered as a resonant background. The gluon-gluon fusion production (ggF H) is simulated using POWHEG 2.0 [43–46]. The vector-boson fusion production (VBF H) and production in association with top quark pairs ($t\bar{t}H$) are simulated using MADGRAPH5_aMC@NLO v2.2.2 (2016) /

v2.4.2 (2017 and 2018). The H production in association with a vector boson (VH) and in association with bottom quarks ($b\bar{b}H$) [47] are simulated using MADGRAPH5_aMC@NLO v2.6.1. The cross sections and decay branching fractions are taken from Ref. [48].

The simulated samples are interfaced with PYTHIA 8 for parton showering and fragmentation with the standard p_T-ordered parton shower scheme. The underlying event is modeled with PYTHIA 8, using the CUETP8M1 (CP5) tune for 2016 (2017, 2018) [49, 50]. Parton distribution functions (PDFs) are taken from the NNPDF3.0 NLO (2016) and NNPDF3.1 NLO (2017, 2018) sets [51–56]. The detector response is modeled using the GEANT4 [57] toolkit. The simulated events include similar additional proton-proton interactions (pileup) as observed in the data with an average of 23–32.

4 Analysis strategy

The final state consists of a pair of photons and a pair of b jets. The pairs correspond to the $H \to \gamma\gamma$ and the $H \to b\bar{b}/Y \to b\bar{b}$ decays, respectively. The invariant mass of two reconstructed Higgs bosons, i.e., $\gamma\gamma b\bar{b}$ 4-body invariant mass, corresponds to the mass of resonance X. The photons and b jets are selected using loose criteria described in Section 4.1, following which, a set of preselection criteria is applied to select events for reconstructing the diphoton and dijet systems. Following this, machine learning algorithms, utilizing the properties of the reconstructed $H \to \gamma\gamma$ and $H \to b\bar{b}$, are used to reject backgrounds, thereby improving the search sensitivity. First, a neural network (NN) training is used to reject the $t\bar{t}H$ background [26] as given in Section 4.2. Second, the nonresonant backgrounds are distinguished from the signal using a boosted decision tree (BDT) discriminant, described in Section 4.3. The events are classified into categories using the BDT discriminant value. The variable $\widetilde{M}_X \equiv m_{\gamma\gamma jj} - m_{\gamma\gamma} - m_{jj} + m_H + m_{H,Y}$, where $m_{\gamma\gamma jj}$ is the invariant mass of $\gamma\gamma b\bar{b}$ system, and m_Y and m_H are the pole masses of Y and H particles [58], is used to further categorize the events (Section 4.4).

The signal is extracted from a simultaneous two-dimensional (2D) fit to the invariant mass of diphoton $m_{\gamma\gamma}$ and dijet m_{jj} systems in all categories. This method benefits from different shapes of $m_{\gamma\gamma}$ and m_{jj} distributions for signal and backgrounds. The signals have peaking $m_{\gamma\gamma}$ and m_{jj} distributions while background events have falling distributions of these observables. In every event category, the signal and background modeling for these observables are performed using the optimized functions as given in Section 4.5.

4.1 Object reconstruction and event preselections

The photons are reconstructed using the ECAL energy deposits. Charged particle tracks are also associated with these energy deposits for converted photons. The ECAL energy is corrected in data using a multivariate regression based on $Z \to ee$ simulation. Photon energy is smeared in simulated events to match the resolution in data [38, 59]. For photon identification, a multivariate identification method (photon ID) based on photon shower shape, isolation, and kinematic variables is used [38]. It separates the signal from background photons. To identify events with two photon objects within ECAL and tracker coverage $|\eta| < 2.5$, they should pass selection on $p_T^\gamma/m_{\gamma\gamma}$ ($p_T^{\gamma_1}/m_{\gamma\gamma} > 1/3$ and $p_T^{\gamma_2}/m_{\gamma\gamma} > 1/4$) and $100 < m_{\gamma\gamma} < 180\,\text{GeV}$, where p_T^γ is transverse momenta of the reconstructed photons.

The primary pp vertex associated with the diphoton system is identified using a multivariate technique as given in Ref. [60]. It has been proven to be 99.9% efficient for correct vertex assignment for $\gamma\gamma b\bar{b}$ final state because of the jet requirement conditions.

After the diphoton vertex reconstruction, events are required to have at least two jets with $p_T > 25\,\text{GeV}$ and $|\eta| < 2.4$ (2.5) for 2016 (2017–2018) that pass jet identification criteria to reject reconstructed jets from calorimeter noise [61]. The selection on the pseudorapidity of jets is looser for 2017–2018 data-taking year because new pixel detector was installed at the beginning of 2017 [62]. The $|\eta|$ selection accepts jets within tracker coverage to identify the b jets using the track information of jets. A $\Delta R = \sqrt{(\Delta\eta)^2 + (\Delta\phi)^2} > 0.4$, ($\phi$ being the azimuthal angle in radians) requirement is applied to have reconstructed photons and jets isolated from each other. For tagging the b jets, the deep neural network and secondary vertex algorithm based tagger DEEPJET [63–65] is used. Further, the jets are corrected with jet energy corrections [66] and b jet energy regression [67]. The b jet energy regression improves the b jet energy resolution, resulting in up to 20% improvement on the m_{jj} resolution. In addition, a wide dijet mass window selection $70 < m_{jj} < 190(1200)\,\text{GeV}$ is also applied depending upon m_{jj} shape of HH (HY) signal. The mass window is kept wider for $X \to HY$ searches to scan over the allowed m_Y region. Within the m_{jj} mass window, a dijet system is reconstructed using the two jets with the highest sum of DEEPJET discriminant score in an event.

4.2 Resonant background rejection

The resonant backgrounds are the different single Higgs productions ($t\bar{t}H$, ggF H, $b\bar{b}H$, VBF H, VH), with peaking $m_{\gamma\gamma}$ distribution around 125 GeV Higgs boson mass, and among them, $t\bar{t}H$ process contributes around 15% of the total resonant background contribution. The ttH background becomes the problematic resonant background because the two top quark decays produce two b quarks which can have an invariant mass m_{jj} near the Higgs boson mass, thus producing similar $m_{\gamma\gamma}$ and m_{jj} distributions to the signal. It is required to minimize the $t\bar{t}H$ contribution to improve results for the low resonance mass region where the analysis is more sensitive than other final state of HH decay. For this purpose, an NN-based discriminant was developed for the nonresonant $HH \to \gamma\gamma b\bar{b}$ analysis [26]. An optimized selection 0.26 on this discriminant rejects 80% $t\bar{t}H$ contribution keeping more than 95% signal efficiency. The same selection is used for this analysis which improves the expected limits in the low mass region by up to 10%. For $m_X > 600\,\text{GeV}$, resonant background contributions become less than 1%, therefore, we do not consider this selection.

The object reconstruction and event preselection criteria are summarized in Table 1.

Table 1: Event preselection criteria

Photons		Jets	
Variable	Requirement	Variable	Requirement
leading photon p_T	$> m_{\gamma\gamma}/3$	p_T	$> 25.\,\text{GeV}$
subleading photon p_T	$> m_{\gamma\gamma}/4$	$\Delta R_{\gamma j}$	> 0.4
$\|\eta\|$	< 2.5	$\|\eta\|$	$< 2.4(2.5)$ for 2016 (2017–2018)
		njets	> 1
$m_{\gamma\gamma}$	100–180 GeV		70–190 GeV for HH and
		m_{jj}	70–1200 GeV for HY jet-pairs with the highest DEEPJET score sum
$t\bar{t}H$ discriminant	≥ 0.26		

4.3 Nonresonant background separation

The dominating nonresonant backgrounds are the SM multijet processes with up to two prompt photons. An MVA based BDT training is performed using simulations to separate signal and

nonresonant backgrounds $\gamma\gamma$ + jets and γ + jets. For this purpose, machine learning tool XGBOOST [68] is used to develop a multi-class BDT classifier.

Within the analysis, various resonant m_X and m_Y hypotheses are studied, which differ in kinematics. Therefore, BDT is trained separately for six different mass ranges to achieve efficient training performance for every signal. In this division, three ranges are in m_X ($m_X < 500$ GeV, m_X in the range 500–700 GeV and $m_X > 700$ GeV) and the rest of three in m_Y ($m_Y < 300$ GeV, $300 < m_Y < 500$ GeV, and $m_Y > 500$ GeV). The bases of the mass range division are the boost factor, defined as $m_X/(m_H + m_Y)$ [69], and the kinematic properties of signal. The boost factor determines the boost of H and Y and the angular distribution of their decay products. Signal events in the same mass range have similar boost factor and kinematic properties, and therefore only one BDT is trained for them inclusively. For the three m_Y ranges, the training was performed using three different but overlapping m_{jj} intervals: 70–400 GeV, 150–560 GeV, and 300–1000 GeV. The mass ranges were optimized taking into account the m_{jj} distributions and the efficiencies of all the signals falling within a particular range. For spin-0 and spin-2 HH searches, the training with m_{jj} interval 70–400 GeV is used since it already covers the phase space with 70–190 GeV selection on m_{jj}.

The simulated $X \to HY$ signal samples are used as training input according to the defined mass ranges and m_{jj} intervals, while simulated nonresonant background events are divided according to the m_{jj} intervals. While training the BDTs for different m_X ranges in the same m_Y range, only signal input changes, background events remain the same. We perform the training for three data-taking years together. The signal cross section is fixed to the same value in every m_X-m_Y range. The nonresonant background simulations of each year are added with normalization to the product of their cross section and luminosity. In the end, the signal and background events are normalized to unity before using as input to the training.

The events are randomized and divided into train and test sets for every training. The input hyperparameters of the training are optimized using the 5-fold cross-validation [70]. An early-stopping feature of XGBOOST is also used to control the over-training. The BDT is trained using the following three groups of input variables along with a year discriminating label:

1) discriminating kinematic variables

- Helicity angles ($|\cos\theta^{CS}_{HY}|$, $|\cos\theta_{jj}|$, $|\cos\theta_{\gamma\gamma}|$), here CS refers to the Collins-Soper frame
- First two minimum angular distance between photons and jets ($\Delta R(\gamma,\text{jets})$)
- $p_T(jj)/m_{\gamma\gamma jj}$ and $p_T(\gamma\gamma)/m_{\gamma\gamma jj}$
- Leading and subleading photons $p_T(\gamma)/m_{\gamma\gamma}$ and jets $p_T(j)/m_{jj}$

2) object identification variables

- Leading and subleading photon ID to reject misidentified photon contribution
- Leading and subleading jet b tagging discriminant from DEEPJET algorithm to reject light jets

3) resolution variables

- Leading and subleading photons resolution variables:
  a) energy resolution (σ_E/E)
  b) mass resolution estimator of the two selected photons ($\sigma_{m_{\gamma\gamma}}/m_{\gamma\gamma}$)
- Leading and subleading jets resolution variables:

a) energy resolution ($\sigma_{p_{\mathrm{T}}(\mathrm{j})} / p_{\mathrm{T}}(\mathrm{j})$)
b) mass resolution ($\sigma_{m_{\mathrm{jj}}} / m_{\mathrm{jj}}$)

The year label is only used to extract training weights separately for different data-taking years. Apart from these variables, pileup density corresponding to each data-taking year is also added as training input. This helps BDT to consider the pileup effect present in real data, while learning the signal and background models. The final BDT discriminating output populates signal events towards high BDT score and background events towards low BDT score.

4.4 Event Classification

We classify events in three different categories based on BDT output along with the selection on $\widetilde{M}_{\mathrm{X}}$ as explained in Sections 4.4.1 and 4.4.2. The optimization of the BDT categories and $\widetilde{M}_{\mathrm{X}}$ mass window remains independent. The $\gamma\gamma\mathrm{b\bar{b}}$ channel suffers from low data statistics due to the high selection efficiency and purity. Therefore, a constraint on background statistics is also used during optimization. The $\widetilde{M}_{\mathrm{X}}$ selection depends on m_{X}, while categorization remains the same for the signals within a m_{X}-m_{Y} mass range.

4.4.1 $\widetilde{M}_{\mathrm{X}}$ mass window selection

By construction, $\widetilde{M}_{\mathrm{X}}$ is 4-body invariant mass where mass resolutions of $m_{\gamma\gamma}$ and m_{jj} are subtracted from $m_{\gamma\gamma\mathrm{jj}}$. It yields better $\widetilde{M}_{\mathrm{X}}$ resolution in comparison to $m_{\gamma\gamma\mathrm{jj}}$. The improvement in $\widetilde{M}_{\mathrm{X}}$ resolution depends on the boost factor of the signal. For the signal, where decay products are in high p_{T} regime, $m_{\gamma\gamma}$ and m_{jj} resolutions are small; hence, their subtraction improves $\widetilde{M}_{\mathrm{X}}$ resolution only around 30%. As we tend to the signal having decay products in low p_{T} regime, $m_{\gamma\gamma}$ and m_{jj} resolutions get large, which subtraction makes this improvement up to 90%.

After $\widetilde{M}_{\mathrm{X}}$ reconstruction, we optimize a tight mass window selection on it for each m_{X} using HH signals. The optimization covers more than 60% of signal events and achieves the best expected results using data from the control region [25]. With good $\widetilde{M}_{\mathrm{X}}$ resolution, this mass window selection helps to reject background keeping the high signal efficiency, thus increasing the signal-to-background ratio.

The optimized mass window on HH signals is directly applied on HY signals. For low m_{Y}, $\widetilde{M}_{\mathrm{X}}$ resolution of HY signals remains similar to HH signals. While for high m_{Y}, $\widetilde{M}_{\mathrm{X}}$ keeps up to 90% improvement in the resolution that gives high signal efficiency with the same mass window. Also, it is checked that the optimized mass window does not significantly affect the correlation between $m_{\gamma\gamma}$ and m_{jj} observables.

4.4.2 MVA categorization

We use signal and nonresonant background simulations to decide categories based on the Punzi figure of merit (FOM) [71] defined as $\epsilon_s/(1+\sqrt{B})$, where ϵ_s is signal efficiency and B refers to background yields. The category optimization remains independent of assuming any signal cross section since Punzi FOM only uses signal efficiency. It prevents categorization bias towards any specific signal hypothesis, and category boundaries remain the same for all signals within a m_{X}-m_{Y} mass range. To serve the same purpose, $\widetilde{M}_{\mathrm{X}}$ selection is not considered during BDT category optimization and applied only during categorization. Therefore, we have six sets of category boundaries corresponding to six training m_{X}-m_{Y} ranges which are summarized in Table 2.

Table 2: Event classification.

	m_Y <300 GeV	m_Y =[300–500] GeV	m_Y >500 GeV
$\widetilde{M}_X$	Mass window	Mass window	Mass window
BDT categories	For m_X <500 GeV CAT 0 = 0.63–1.0 CAT 1 = 0.33–0.63 CAT 2 = 0.17–0.33 For m_X =[500–700] GeV CAT 0 = 0.55–1.0 CAT 1 = 0.40–0.55 CAT 2 = 0.21–0.40 For m_X >700 GeV CAT 0 = 0.50–1.0 CAT 1 = 0.30–0.50 CAT 2 = 0.21–0.30	For m_X =[500–700] GeV CAT 0 = 0.60–1.0 CAT 1 = 0.35–0.60 CAT 2 = 0.18–0.35 m_X >700 GeV CAT 0 = 0.35–1.0 CAT 1 = 0.24–0.35 CAT 2 = 0.18–0.24	MX>700 GeV CAT 0 = 0.40–1.0 CAT 1 = 0.29–0.40 CAT 2 = 0.13–0.29

The optimization study is performed using a ROOT package Minuit [72] with MIGrad minimizer. First, the BDT output is transformed to have a uniform signal event density for the entire BDT output range, making the categorization easier. The transformation is applied to both data and simulations. The minimizer decides boundaries on BDT output to get the maximum root-square-sum of Punzi FOM from all categories. Four boundaries are provided by this optimization, among which the background-dominated BDT region is always discarded, and the rest of the three are considered. These categories are labeled as CAT 0, CAT 1 and CAT 2 depending upon the value of Punzi FOM. For CAT 0, CAT 1 and CAT 2, Punzi FOM ranges 0.01–0.05, 0.003–0.02 and 0.001–0.006, respectively. For $m_X < 500$ GeV and $m_Y < 300$ GeV mass range, we get the minimum value of Punzi FOM due to the very high background contribution compared to other mass ranges.

4.5 Signal and background modeling

For signal extraction, a parametric fit in the ($m_{\gamma\gamma}$, m_{jj}) plane is performed for every category. The final signal and background templates are the product of the independent $m_{\gamma\gamma}$ and m_{jj} models. For signal and resonant backgrounds, templates are made using simulations, while for templates of the nonresonant backgrounds, the $m_{\gamma\gamma}$ and m_{jj} distributions in data are used. The m_{jj} fit range for HY searches with $m_Y < 200$ GeV are kept as the same as HH searches.

For signal modeling, categorized events are fitted with a product of two parametric signal models: A sum of Gaussian distributions for $m_{\gamma\gamma}$ and a double-sided Crystal Ball (CB) or sum of CB and Gaussian function for m_{jj}. The $m_{\gamma\gamma}$ shape is parameterized using the sum of up to five Gaussian functions. The possible correlations are calculated using the 2D distributions of the observables from simulated signal samples and found to be negligible within the statistical precision of this analysis.

To model the resonant single Higgs background, the $m_{\gamma\gamma}$ shape is constructed from the simulation following the same methodology used for the signal model. The m_{jj} modeling depends on the production mechanism of single H process, and a parameterization is obtained from the simulated distributions: for the ggF H and VBF H processes, the m_{jj} distribution is modeled with a Bernstein polynomial; for VH production, a CB function is used to model the distribu-

tion of the hadronic decays of vector bosons; for $t\bar{t}H$, where the two b jets are produced from a top quark decay, a Gaussian function with a mean around 120 GeV is used.

The nonresonant background model is extracted from data using the discrete profiling method described in Ref. [60, 73]. This technique estimates the systematic uncertainty associated with the choice of the analytic function to fit the background $m_{\gamma\gamma}$ and m_{jj} distributions and treats the background function as a discrete nuisance parameter in the likelihood fit to the data. For background modeling, events with $m_{\gamma\gamma}$ side-band are considered. The final choice of background model is validated using the bias-test [74].

5 Systematic uncertainties

The impact of several sources of systematic uncertainties is studied in the analysis. The systematic uncertainties affect mainly the signal and the resonant single Higgs background. The nonresonant background model is constructed using a data-driven method; the uncertainties associated with the choice of background fit function are taken into account by the discrete profiling method described in Section 4.5. Systematic uncertainties can affect normalization and $m_{\gamma\gamma}$, m_{jj} shapes of signal and single Higgs background models. Systematic uncertainties modifying the shape of the $m_{\gamma\gamma}$ distribution are built in the models as parametric nuisance parameters. The systematic experimental uncertainties are studied separately for each category, and dominant sources among them are:

- *Jet energy scale and smearing corrections*: These are measured using p_T balance of jets with respect to Z and photons in $Z \to ee$, $Z \to \mu\mu$ and $\gamma +$ jets events [33, 75]. The uncertainties vary from 1–2% depending upon the p_T and η of jets. The impact is evaluated by varying the corrections within their uncertainties and propagating them to the final result.
- *Jet b tagging*: Reshaping scale factors (SFs) are used to correct the shape of DEEPJET discriminant coming from simulation to match with data. These depend on p_T, η and the flavor of the jets. The uncertainty associated with this SFs measurement is obtained by comparing b discriminant distribution between data and simulation [63]. The impacts from different systematic uncertainty sources are studied and found to be highest where the light flavor jet gets misidentified as b jet. The average size of uncertainty varies from 4–6%.
- *Integrated luminosity*: These are included from CMS recommendations [35–37]. It ranges from 1–2.5% for 2016–2018 data-taking years and has a combined impact of 1.6%. The possible correlations from different common sources of luminosity measurements are taken into account.
- *Trigger efficiency*: It is calculated with the tag-and-probe method using $Z \to ee$ events. Its average size is around 1–2% and the impact on the final result is less than 1%. More details are given in Ref. [76].
- *Photon preselection uncertainty*: It is studied on the ratio of efficiency measured in data and simulation after passing the preselections. The tag-and-probe method is used for data preselection efficiency on $Z \to ee$ events [76]. Overall it has an impact of less than 1% on the final results.
- *Photon energy scale and resolution*: These uncertainties are studied on $Z \to ee$ events and directly applied on data for scale corrections and simulation for resolution corrections [77].

- *QCD scale*: This uncertainty is related to the variation in renormalization and factorization scales. In order to estimate the scale uncertainty, simulation samples are used to compute the variation in acceptance with respect to the QCD scale. For signal, its size goes up to 5%. It is treated as fully correlated across three data-taking years.

The impact of other systematic sources is small. The highest impact is found on the low resonance masses with 1–2%. The uncertainties on the QCD scale and b tagging are the most dominated systematic uncertainties impacting all the mass ranges.

6 Results

For 2D $m_{\gamma\gamma} : m_{\mathrm{jj}}$ fit signal extraction method, a likelihood function is defined using signal and background analytic models of $m_{\gamma\gamma}$ and m_{jj} distributions, optimized in Section 4.5, with nuisance parameters related to the uncertainties explained in Section 5. A simultaneous unbinned maximum likelihood fit to the $m_{\gamma\gamma}$ and m_{jj} observable distributions is performed within three categories to extract the signal. Figures 2 and 3 represent the data and signal-plus-background fit for $m_{\gamma\gamma}$ and m_{jj} observables in CAT 0. No deviation is observed from the background-only hypothesis. Therefore, we set the upper limit at 95% CL on the product of resonant production cross section and branching ratio to $\gamma\gamma\mathrm{b\bar{b}}$ channel using the modified frequentist approach for confidence levels (CLs), taking the LHC profile likelihood ratio as a test statistic in the asymptotic approximation [78–81].

Figure 4 shows the upper limits on resonant production cross section as a function of resonance mass m_{X} for HH searches. Expected limits decrease from low to high m_{X} region and observed limits are consistent with them within 2σ deviation. Depending upon m_{X}, the observed upper limits at 95% CL vary between 0.82–0.07 fb and 0.78–0.06 fb for spin-0 and spin-2 resonant HH searches, respectively. The corresponding expected ranges are 0.74–0.08 fb and 0.65–0.06 fb, respectively. These results exclude masses up to 600 GeV for spin-0 bulk radion signal at $\Lambda_R = 6$ TeV and up to 850 GeV for spin-2 bulk KK graviton signal with coupling factor $\kappa/\overline{M_{pl}} = 0.5$.

Figure 5 describes the upper limits at 95% CL for $\mathrm{pp} \to \mathrm{X} \to \mathrm{HY} \to \gamma\gamma\mathrm{b\bar{b}}$ signal as function on m_{Y} with different m_{X} hypotheses. For good representation of the results, the limits are scaled with the order of 10 with different m_{X} hypotheses as labeled in the figure. For every m_{X}, the expected limits first improve and then start rising up with the high m_{Y} region. This is because of the high boost where objects can not be treated as well-separated and this resolved analysis starts losing the search sensitivity. Observed limits remain consistent with the expected limits within 2σ deviation except for $m_{\mathrm{X}} = 650$ GeV with $m_{\mathrm{X}} <= 100$ GeV. The observed and expected limits vary between 0.90–0.04 fb and 0.79–0.05 fb depending upon the mass ranges in m_{X} and m_{Y}, respectively. The limits for m_{X} points with range 300–1000 GeV in steps of 100 GeV are obtained using simulations while the limits for intermediate m_{X} points 350–950 GeV in steps of 100 GeV are obtained using the signal models made from interpolation of signal fit parameters and normalization. This approach is validated for a signal we have in simulation by comparing the limits we get from the simulation and from the interpolation methods.

The largest excess of the observation from the estimated background occurs for $m_{\mathrm{X}} = 650$ GeV and $m_{\mathrm{Y}} = 90$ GeV with a local significance of 3.8 standard deviations while an excess of local significance of 3.5 standard deviations is observed for $m_{\mathrm{X}} = 650$ GeV and $m_{\mathrm{Y}} = 100$ GeV. The best fit value of the product of the cross section with the branching fraction for the decay into $\gamma\gamma\mathrm{b\bar{b}}$ at the largest excess is $\sigma(\mathrm{pp} \to \mathrm{X} \to \mathrm{HY} \to \gamma\gamma\mathrm{b\bar{b}}) = (0.35 \pm {}^{0.17}_{0.13})$ fb. Taking into account the "Look elsewhere effect" [82] for m_{X} range 300–1000 GeV and m_{Y} range 90–150 GeV, the global significance reduces to 2.8 standard deviations, with a corresponding p-value of 0.0027.

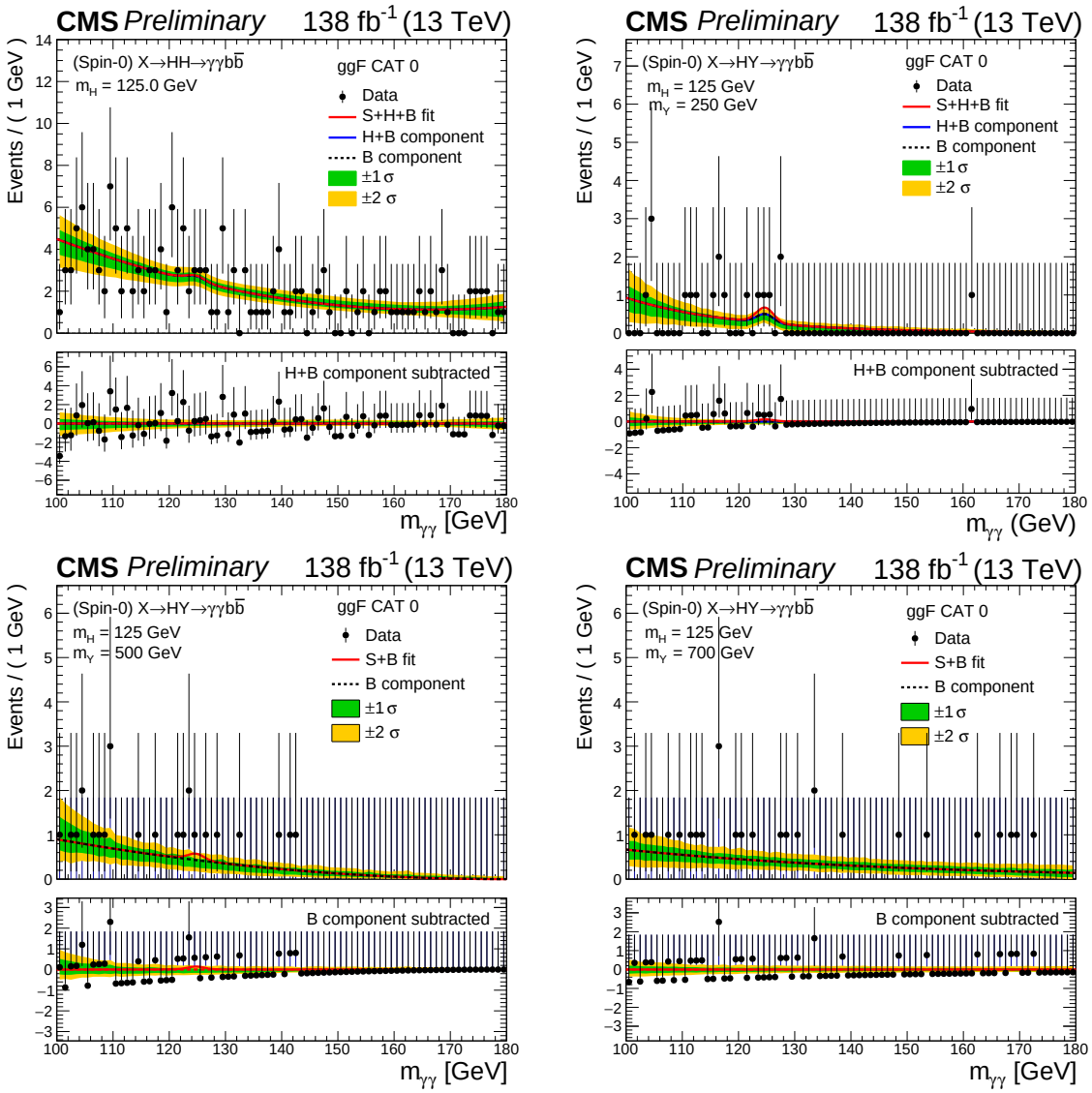

Figure 2: Invariant mass distributions $m_{\gamma\gamma}$ with the selected data events (black points) for the signal dominated category (CAT 0). The upper left plot represents HH signal and rest of three represent HY signal with m_{Y} =250, 500 and 700 GeV mass hypotheses, respectively. The solid red line shows the sum of the fitted signal and background events. The solid blue line shows the total background component by summing the resonant and nonresonant background contributions and the dashed black line shows the nonresonant background component. The green and yellow bands represent the 1 and 2 standard deviations which include the uncertainties in fit to the background component. The lower panel in each plot shows the residual signal yield after the background subtraction.

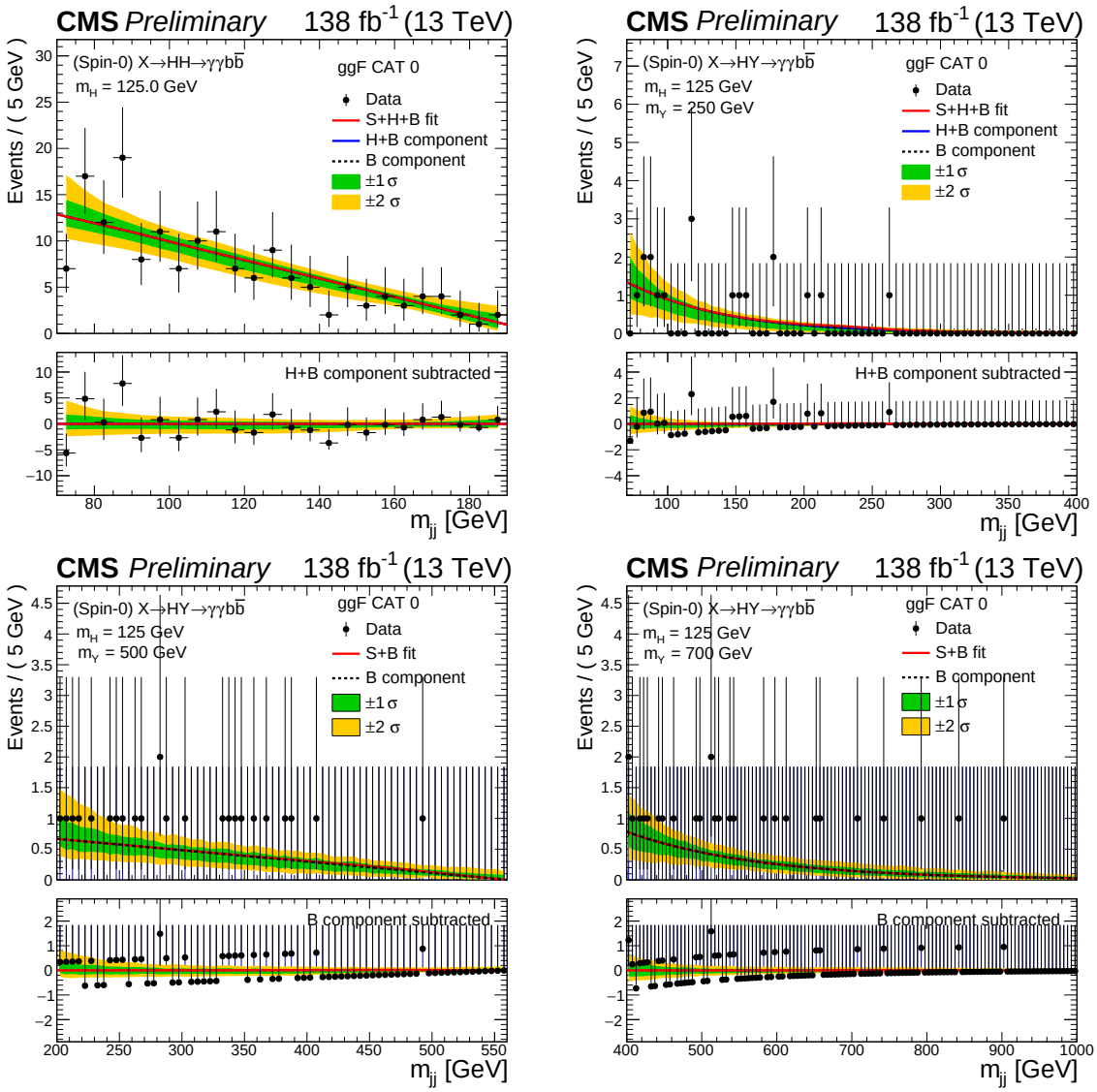

Figure 3: Invariant mass distributions m_{jj} with the selected data events (black points) for the signal dominated category (CAT 0). The upper left plot represents HH signal and rest of three represent HY signal with m_Y =250, 500 and 700 GeV mass hypotheses, respectively. The solid red line shows the sum of the fitted signal and background events. The solid blue line shows the total background component by summing the resonant and nonresonant background contributions and the dashed black line shows the nonresonant background component. The green and yellow bands represent the 1 and 2 standard deviations which include the uncertainties in fit to the background component. The lower panel in each plot shows the residual signal yield after the background subtraction.

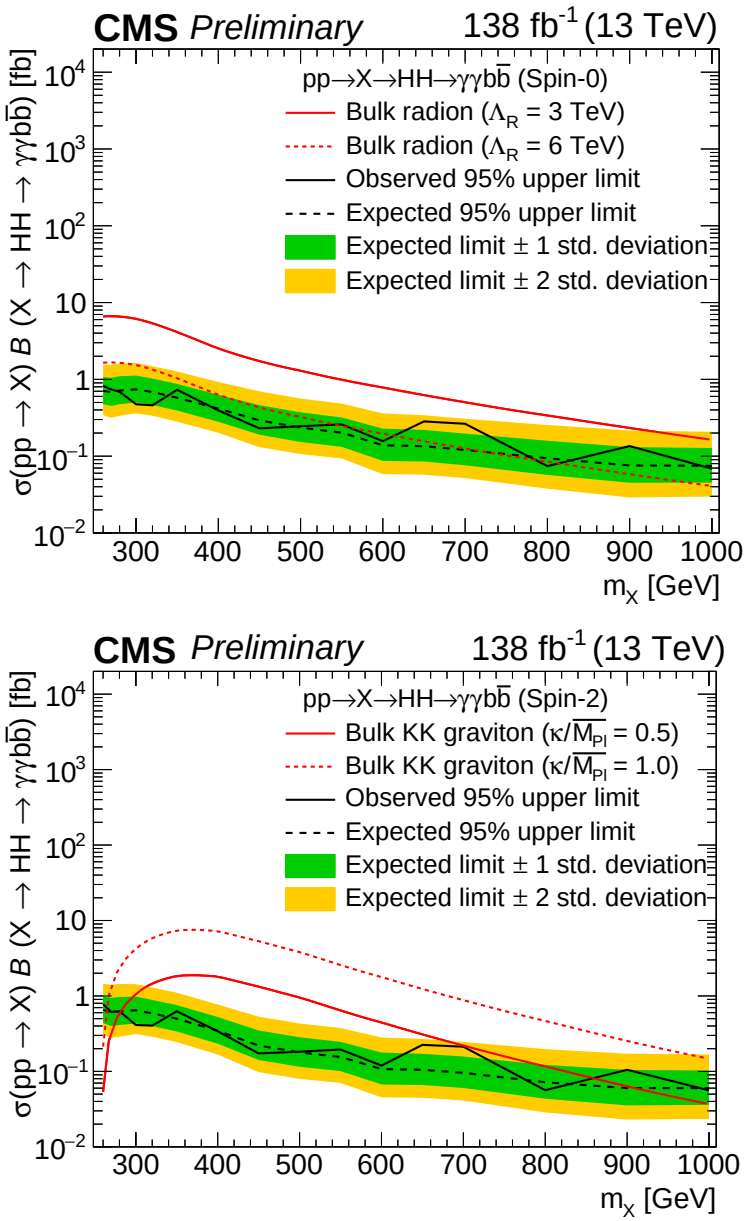

Figure 4: Expected and observed 95% CL upper limit on product of resonant production cross section and branching fraction for spin-0 (upper plot) and spin-2 (lower plot) pp $\rightarrow$ X $\rightarrow$ HH $\rightarrow$ $\gamma\gamma$b$\bar{\text{b}}$ signal hypotheses. The dashed and solid black lines represent expected and observed limits, respectively. The green and yellow bands represent the 1 and 2 standard deviations for the expected limit. The red lines show the theoretical predictions with different energy scales and couplings.

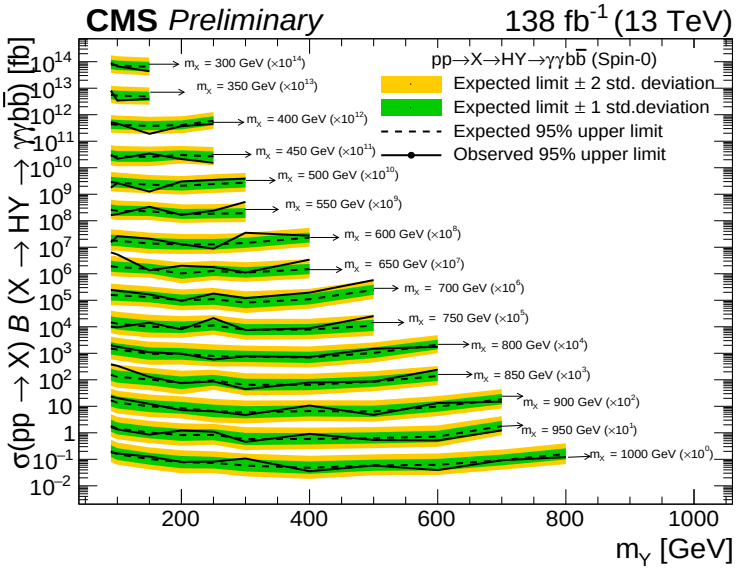

Figure 5: The upper plot shows the expected and observed 95% CL exclusion limit on production cross section for $pp \to X \to HY \to \gamma\gamma b\bar{b}$ signal hypothesis. The dashed and solid black lines represent expected and observed limits, respectively. The green and yellow bands represent the 1 and 2 standard deviations for the expected limit. Limits are scaled with the order of 10 depending upon m_X.

The largest excess, for m_Y within its resolution, is consistent with the previous searches made by the CMS collaboration where excess is reported for resonances decaying into the $\tau\tau$ final state and for the high-mass resonances decaying into the WW using 13 TeV LHC data collected during 2016, 2017 and 2018 data-taking periods, corresponding to an integrated luminosity of 138 fb^{-1} [83, 84]. It also coincides with a similar excess observed in previous search for low-mass resonances in the $\gamma\gamma$ final state by the CMS collaboration using data collected during 2016 (2012) data-taking year with an integrated luminosity of 35.9 (19.7) fb^{-1} [85]. An updated search including 2017–2018 LHC data is in progress for this analysis.

Figure 6 shows the expected and observed upper limits at 95% CL on the product of the signal production cross section and the branching fraction $pp \to X \to HY \to \gamma\gamma b\bar{b}$, and compares them with the maximally allowed cross sections from the NMSSM and TRSM models. For NMSSM, the expected and observed limits exclude masses between 400–650 GeV in m_X and 90–300 GeV in m_Y. In the TRSM interpretation, the excluded mass region covers an area with 300-500 GeV in m_X for the expected limits and with 300-550 GeV for the observed limits while the mass exclusion in m_Y remains 90–150 GeV for both the limits. The m_X beyond 1 TeV is not studied because of the significantly better sensitivity of the $b\bar{b}b\bar{b}$ channel for HH searches in this mass region [86].

7 Summary

A search for new resonances X decaying either to a pair of Higgs bosons HH, or to a Higgs boson and a new scalar Y, is presented. The search uses data from proton-proton collisions collected by the CMS experiment at LHC in 2016–2018 at a center-of-mass energy of 13 TeV, and corresponding to 138 fb^{-1} of integrated luminosity. The study is motivated from theories related to the warped extra dimension model, the next-to-minimal supersymmetric standard

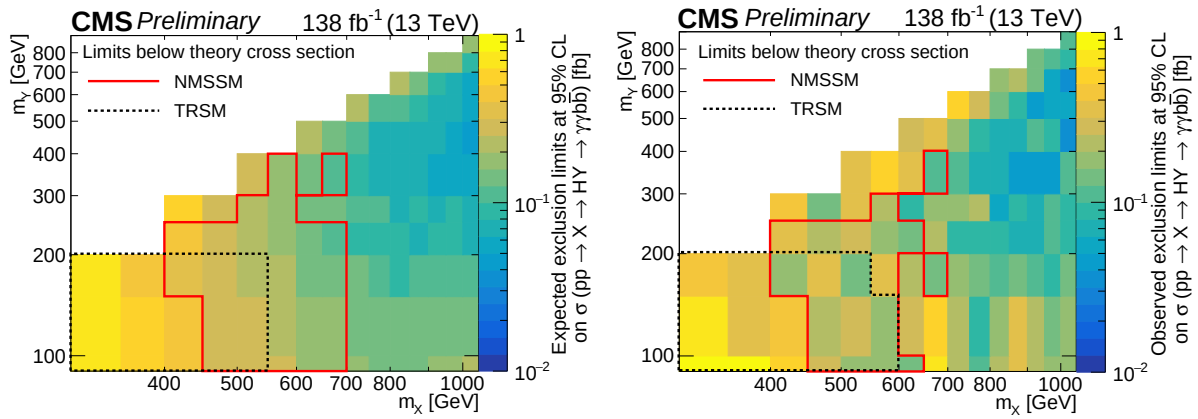

Figure 6: Comparison of the expected (left) and observed (right) limits at 95% CL with the maximally allowed cross sections from NMSSM and TRSM models where the red and black lines indicate the excluded mass regions for both, respectively.

model and the two-real-scalar-singlet model assuming narrow width approximation. For a X decaying to HH, a mass range of 260 GeV–1 TeV is covered, while a X decaying to HY is searched for range 300 GeV–1 TeV in m_X, considering a mass range 90–800 GeV in m_Y. The data were found to be compatible with the background-only hypothesis. Results are presented as the upper limits at 95% confidence level on the product of the production cross section of X and its branching fraction to the $\gamma\gamma b\bar{b}$ final state, through either HH or HY. Depending upon the mass range in m_X, the observed limits for a spin-0 resonance X, decaying to HH, ranges from 0.82–0.07 fb, while the expected limits are 0.74–0.08 fb. Bulk radions decaying to HH are excluded for masses up to 600 GeV for $\Lambda_R = 6$ TeV, while the mass limit on a bulk KK graviton extends to 850 GeV assuming a coupling factor $\kappa/\overline{M_{pl}} = 0.5$. For the resonance X decaying to HY, the observed limits are 0.90–0.04 fb, while the expected limits lie in the range 0.79–0.05 fb, depending upon the mass ranges in m_X and m_Y. The largest deviation from background-only hypothesis with local (global) significance of 3.8 (2.8) standard deviations is also observed for m_X = 650 GeV and m_Y = 90 GeV. The results are interpreted for the NMSSM and the TRSM theories.

References

[1] ATLAS Collaboration, "Observation of a new particle in the search for the standard model Higgs boson with the ATLAS detector at the LHC", *Phys. Lett. B* **716** (2012) 1, doi:10.1016/j.physletb.2012.08.020, arXiv:1207.7214.

[2] CMS Collaboration, "Observation of a new boson at a mass of 125 GeV with the CMS experiment at the LHC", *Phys. Lett. B* **716** (2012) 30, doi:10.1016/j.physletb.2012.08.021, arXiv:1207.7235.

[3] CMS Collaboration, "Observation of a new boson with mass near 125 GeV in pp collisions at $\sqrt{s}$ = 7 and 8 TeV", *JHEP* **06** (2013) 081, doi:10.1007/JHEP06(2013)081, arXiv:1303.4571.

[4] S. Weinberg, "A model of leptons", *Phys. Rev. Lett.* **19** (1967) 1264, doi:10.1103/PhysRevLett.19.1264.

[5] Sheldon L. Glashow, "Partial-symmetries of weak interactions", *Nuclear Physics* **22** (1961) 579, doi:10.1016/0029-5582(61)90469-2.

[6] G. 't Hooft and M. Veltman, "Regularization and renormalization of gauge fields", *Nuclear Physics B* **44** (1972) doi:10.1016/0550-3213(72)90279-9.

[7] P. W. Higgs, "Broken symmetries, massless particles and gauge fields", *Phys. Lett.* **12** (1964) 132, doi:10.1016/0031-9163(64)91136-9.

[8] P. W. Higgs, "Broken symmetries and the masses of gauge bosons", *Phys. Rev. Lett.* **13** (1964) 508, doi:10.1103/PhysRevLett.13.508.

[9] CMS Collaboration, "A measurement of the Higgs boson mass in the diphoton decay channel", *Phys. Lett. B* **805** (2020) 135425, doi:10.1016/j.physletb.2020.135425, arXiv:2002.06398.

[10] L. Randall and R. Sundrum, "Large mass hierarchy from a small extra dimension", *Phys. Rev. Lett.* **83** (1999) 3370, doi:10.1103/PhysRevLett.83.3370, arXiv:hep-ph/9905221.

[11] W. D. Goldberger and M. B. Wise, "Modulus stabilization with bulk fields", *Phys. Rev. Lett.* **83** (1999) 4922, doi:10.1103/PhysRevLett.83.4922, arXiv:hep-ph/9907447.

[12] C. Csáki, M. Graesser, L. Randall, and J. Terning, "Cosmology of brane models with radion stabilization", *Phys. Rev. D* **62** (2000) 045015, doi:10.1103/PhysRevD.62.045015, arXiv:hep-ph/9911406.

[13] C. Csáki, M. L. Graesser, and G. D. Kribs, "Radion dynamics and electroweak physics", *Phys. Rev. D* **63** (2001) 065002, doi:10.1103/PhysRevD.63.065002, arXiv:hep-th/0008151.

[14] H. Davoudiasl, J. L. Hewett, and T. G. Rizzo, "Phenomenology of the Randall–Sundrum Gauge Hierarchy Model", *Phys. Rev. Lett.* **84** (2000) 2080, doi:10.1103/PhysRevLett.84.2080, arXiv:hep-ph/9909255.

[15] O. DeWolfe, D. Z. Freedman, S. S. Gubser, and A. Karch, "Modeling the fifth dimension with scalars and gravity", *Phys. Rev. D* **62** (2000) 046008, doi:10.1103/PhysRevD.62.046008, arXiv:hep-th/9909134.

[16] K. Agashe, H. Davoudiasl, G. Perez, and A. Soni, "Warped gravitons at the CERN LHC and beyond", *Phys. Rev. D* **76** (2007) 036006, doi:10.1103/PhysRevD.76.036006, arXiv:hep-ph/0701186.

[17] Yu. A. Golfand and E. P. Likhtman, "Extension of the algebra of Poincaré group generators and violation of p invariance", *JETP Lett.* **13** (1971) 323, doi:10.1142/9789814542340_0001.

[18] J. Wess and B. Zumino, "Supergauge transformations in four-dimensions", *Nucl. Phys. B* **70** (1974) 39, doi:10.1016/0550-3213(74)90355-1.

[19] P. Fayet, "Supergauge invariant extension of the Higgs mechanism and a model for the electron and its neutrino", *Nucl. Phys. B* **90** (1975) 104, doi:10.1016/0550-3213(75)90636-7.

[20] P. Fayet, "Spontaneously broken supersymmetric theories of weak, electromagnetic and strong interactions", *Phys. Lett. B* **69** (1977) 489, doi:10.1016/0370-2693(77)90852-8.

[21] U. Ellwanger, C. Hugonie, and A. M. Teixeira, "The Next-to-Minimal Supersymmetric Standard Model", *Phys. Rept.* **496** (2010) 1, doi:10.1016/j.physrep.2010.07.001, arXiv:0910.1785.

[22] M. Maniatis, "The Next-to-Minimal Supersymmetric extension of the Standard Model reviewed", *Int. J. Mod. Phys. A* **25** (2010) 3505, doi:10.1142/S0217751X10049827, arXiv:0906.0777.

[23] J. E. Kim and H. P. Nilles, "The μ-problem and the strong CP problem", *Phys. Lett. B* **138** (1984) 150, doi:10.1016/0370-2693(84)91890-2.

[24] T. Robens, T. Stefaniak, and J. Wittbrodt, "Two-real-scalar-singlet extension of the SM: LHC phenomenology and benchmark scenarios", *Eur. Phys. J. C* **80** (2020) 151, doi:10.1140/epjc/s10052-020-7655-x, arXiv:1908.08554.

[25] CMS Collaboration, "Search for Higgs boson pair production in the $\gamma\gamma b\bar{b}$ final state in pp collisions at $\sqrt{s} = 13$ TeV", *Phys. Lett. B* **788** (2019) 7, doi:10.1016/j.physletb.2018.10.056, arXiv:1806.00408.

[26] CMS Collaboration, "Search for nonresonant Higgs boson pair production in final states with two bottom quarks and two photons in proton-proton collisions at $\sqrt{s}$ = 13 TeV", *JHEP* **03** (2021) 257, doi:10.1007/JHEP03(2021)257, arXiv:2011.12373.

[27] CMS Collaboration, "The CMS experiment at the CERN LHC", *JINST* **3** (2008) S08004, doi:10.1088/1748-0221/3/08/S08004.

[28] CMS Collaboration, "The CMS trigger system", *JINST* **12** (2017) P01020, doi:10.1088/1748-0221/12/01/P01020, arXiv:1609.02366.

[29] CMS Collaboration, "The CMS high level trigger", *Eur. Phys. J. C* **46** (2006) 605, doi:10.1140/epjc/s2006-02495-8, arXiv:hep-ex/0512077.

[30] CMS Collaboration, "Particle-flow reconstruction and global event description with the cms detector", *JINST* **12** (2017) P10003, doi:10.1088/1748-0221/12/10/P10003, arXiv:1706.04965.

[31] M. Cacciari, G. P. Salam, and G. Soyez, "The anti-k_T jet clustering algorithm", *JHEP* **04** (2008) 063, doi:10.1088/1126-6708/2008/04/063, arXiv:0802.1189.

[32] M. Cacciari, G. P. Salam, and G. Soyez, "FastJet user manual", *Eur. Phys. J. C* **72** (2012) 1896, doi:10.1140/epjc/s10052-012-1896-2, arXiv:1111.6097.

[33] CMS Collaboration, "Jet energy scale and resolution in the CMS experiment in pp collisions at 8 TeV", *JINST* **12** (2017) P02014, doi:10.1088/1748-0221/12/02/P02014, arXiv:1607.03663.

[34] CMS Collaboration, "Performance of missing transverse momentum reconstruction in proton-proton collisions at $\sqrt{s} = 13$ TeV using the CMS detector", *JINST* **14** (2019) P07004, doi:10.1088/1748-0221/14/07/P07004, arXiv:1903.06078.

[35] CMS Collaboration, "Precision luminosity measurement in proton-proton collisions at $\sqrt{s} = 13$ TeV in 2015 and 2016 at CMS", *Eur. Phys. J. C* **81** (2021) 800, doi:10.1140/epjc/s10052-021-09538-2, arXiv:2104.01927.

[36] CMS Collaboration, "CMS luminosity measurement for the 2017 data taking period at $\sqrt{s} = 13\,\text{TeV}$", CMS Physics Analysis Summary CMS-PAS-LUM-17-004, CERN, 2018.

[37] CMS Collaboration, "CMS luminosity measurement for the 2018 data-taking period at $\sqrt{s} = 13\,\text{TeV}$", CMS Physics Analysis Summary CMS-PAS-LUM-18-002, CERN, 2019.

[38] CMS Collaboration, "Measurements of Higgs boson properties in the diphoton decay channel in proton-proton collisions at $\sqrt{s} = 13$ TeV", *JHEP* **11** (2018) 185, doi:10.1007/JHEP11(2018)185, arXiv:1804.02716.

[39] J. Alwall et al., "The automated computation of tree-level and next-to-leading order differential cross sections, and their matching to parton shower simulations", *JHEP* **07** (2014) 079, doi:10.1007/JHEP07(2014)079, arXiv:1405.0301.

[40] A. Alloul et al., "FeynRules 2.0 - A complete toolbox for tree-level phenomenology", *Comput. Phys. Commun.* **185** (2014) 2250, doi:10.1016/j.cpc.2014.04.012, arXiv:1310.1921.

[41] T. Gleisberg et al., "Event generation with SHERPA 1.1", *JHEP* **02** (2009) 007, doi:10.1088/1126-6708/2009/02/007, arXiv:0811.4622.

[42] T. Sjöstrand et al., "An introduction to PYTHIA 8.2", *Comput. Phys. Commun.* **191** (2015) 159, doi:10.1016/j.cpc.2015.01.024, arXiv:1410.3012.

[43] P. Nason, "A new method for combining NLO QCD with shower Monte Carlo algorithms", *JHEP* **11** (2004) 040, doi:10.1088/1126-6708/2004/11/040, arXiv:hep-ph/0409146.

[44] S. Frixione, P. Nason, and C. Oleari, "Matching NLO QCD computations with Parton Shower simulations: the POWHEG method", *JHEP* **11** (2007) 070, doi:10.1088/1126-6708/2007/11/070, arXiv:0709.2092.

[45] S. Alioli, P. Nason, C. Oleari, and E. Re, "A general framework for implementing NLO calculations in shower Monte Carlo programs: the POWHEG BOX", *JHEP* **06** (2010) 043, doi:10.1007/JHEP06(2010)043, arXiv:1002.2581.

[46] E. Bagnaschi, G. Degrassi, P. Slavich, and A. Vicini, "Higgs production via gluon fusion in the POWHEG approach in the SM and in the MSSM", *JHEP* **02** (2012) 088, doi:10.1007/JHEP02(2012)088, arXiv:1111.2854.

[47] M. Wiesemann et al., "Higgs production in association with bottom quarks", *JHEP* **02** (2015) doi:10.1007/jhep02(2015)132.

[48] D. de Florian et al., "Handbook of LHC Higgs cross sections: 4. Deciphering the nature of the Higgs sector", 2016. arXiv:1610.07922. CERN-2017-002-M.

[49] CMS Collaboration, "Event generator tunes obtained from underlying event and multiparton scattering measurements", *Eur. Phys. J. C* **76** (2016) 155, doi:10.1140/epjc/s10052-016-3988-x, arXiv:1512.00815.

[50] CMS Collaboration, "Extraction and validation of a new set of CMS PYTHIA8 tunes from underlying-event measurements", *Eur. Phys. J. C* **80** (2020) 4, doi:10.1140/epjc/s10052-019-7499-4, arXiv:1903.12179.

[51] NNPDF Collaboration, "Parton distributions for the LHC Run II", *JHEP* **04** (2015) 040, doi:10.1007/JHEP04(2015)040, arXiv:1410.8849.

[52] NNPDF Collaboration, "Parton distributions from high-precision collider data", *Eur. Phys. J. C* **77** (2017) 663, doi:10.1140/epjc/s10052-017-5199-5, arXiv:1706.00428.

[53] S. Carrazza, J. I. Latorre, J. Rojo, and G. Watt, "A compression algorithm for the combination of PDF sets", *Eur. Phys. J. C* **75** (2015) 474, doi:10.1140/epjc/s10052-015-3703-3, arXiv:1504.06469.

[54] J. Butterworth et al., "PDF4LHC recommendations for LHC Run II", *J. Phys. G* **43** (2016) 023001, doi:10.1088/0954-3899/43/2/023001, arXiv:1510.03865.

[55] S. Dulat et al., "New parton distribution functions from a global analysis of quantum chromodynamics", *Phys. Rev. D* **93** (2016) 033006, doi:10.1103/PhysRevD.93.033006, arXiv:1506.07443.

[56] L. A. Harland-Lang, A. D. Martin, P. Motylinski, and R. S. Thorne, "Parton distributions in the LHC era: MMHT 2014 PDFs", *Eur. Phys. J. C* **75** (2015) 204, doi:10.1140/epjc/s10052-015-3397-6, arXiv:1412.3989.

[57] GEANT4 Collaboration, "GEANT4—a simulation toolkit", *Nucl. Instrum. Meth. A* **506** (2003) 250, doi:10.1016/S0168-9002(03)01368-8.

[58] N. Kumar and S. P. Martin, "LHC search for di-Higgs decays of stoponium and other scalars in events with two photons and two bottom jets", *Phys. Rev. D* **90** (2014) 055007, doi:10.1103/PhysRevD.90.055007, arXiv:1404.0996.

[59] E. Spyromitros-Xioufis, G. Tsoumakas, W. Groves, and I. Vlahavas, "Multi-target regression via input space expansion: treating targets as inputs", *Machine Learning* **104** (2016) 55, doi:10.1007/s10994-016-5546-z, arXiv:1211.6581.

[60] CMS Collaboration, "Observation of the diphoton decay of the Higgs boson and measurement of its properties", *Eur. Phys. J. C* **74** (2014) 3076, doi:10.1140/epjc/s10052-014-3076-z, arXiv:1407.0558.

[61] CMS Collaboration, "Pileup mitigation at CMS in 13 TeV data", *JINST* **15** (2020) P09018, doi:10.1088/1748-0221/15/09/P09018, arXiv:2003.00503.

[62] B. Vormwald, "The CMS phase-1 pixel detector - experience and lessons learned from two years of operation", *JINST* **14** (2019) C07008, doi:10.1088/1748-0221/14/07/c07008.

[63] CMS Collaboration, "Identification of heavy-flavour jets with the CMS detector in pp collisions at 13 TeV", *JINST* **13** (2018) P05011, doi:10.1088/1748-0221/13/05/P05011, arXiv:1712.07158.

[64] E. Bols et al., "Jet Flavour Classification Using DeepJet", *JINST* **15** (2020) P12012, doi:10.1088/1748-0221/15/12/P12012, arXiv:2008.10519.

[65] CMS Collaboration, "Performance of the DeepJet b tagging algorithm using 41.9/fb of data from proton-proton collisions at 13 TeV with Phase 1 CMS detector", CMS Detector Performance Note CMS-DP-2018-058, CERN, 2018.

[66] CMS Collaboration, "Determination of jet energy calibration and transverse momentum resolution in CMS", *JINST* **6** (2011) P11002, doi:10.1088/1748-0221/6/11/P11002, arXiv:1107.4277.

[67] CMS Collaboration, "A deep neural network for simultaneous estimation of b jet energy and resolution", *Comput. Softw. Big Sci.* **4** (2020) 10, doi:10.1007/s41781-020-00041-z, arXiv:1912.06046.

[68] T. Chen and C. Guestrin, "XGBoost: A scalable tree boosting system", in *Proceedings of the 22nd ACM SIGKDD International Conference on Knowledge Discovery and Data Mining*, KDD, p. 785. ACM, New York, NY, USA, 2016. doi:10.1145/2939672.2939785.

[69] M. Gouzevitch et al., "Scale-invariant resonance tagging in multijet events and new physics in Higgs pair production", *JHEP* **07** (2013) 148, doi:10.1007/JHEP07(2013)148, arXiv:1303.6636.

[70] T. Hastie, R. Tibshirani, and J. Friedman, "The elements of statistical learning". Springer-Verlag New York, 2nd edition, 2009. doi:10.1007/978-0-387-84858-7.

[71] G. Punzi, "Sensitivity of searches for new signals and its Optimization", in *Statistical Problems in Particle Physics, Astrophysics, and Cosmology*, L. Lyons, R. Mount, and R. Reitmeyer, eds., p. 79. January, 2003. arXiv:physics/0308063.

[72] R. Brun and F. Rademakers, "ROOT: An object oriented data analysis framework", *Nucl. Instrum. Meth. A* **389** (1997) 81, doi:10.1016/S0168-9002(97)00048-X.

[73] P. D. Dauncey, M. Kenzie, N. Wardle, and G. J. Davies, "Handling uncertainties in background shapes: the discrete profiling method", *JINST* **10** (2015) P04015, doi:10.1088/1748-0221/10/04/P04015, arXiv:1408.6865.

[74] D. L. H.-V. Richard G. Lomax, "Statistical Concepts - A Second Course". Routledge New York, 4th edition, 2012. doi:10.4324/9780203137802.

[75] CMS Collaboration, "Jet algorithms performance in 13 TeV data", CMS Physics Analysis Summary CMS-PAS-JME-16-003, CERN, 2017.

[76] CMS Collaboration, "Measurement of the Inclusive W and Z Production Cross Sections in pp Collisions at $\sqrt{s} = 7$ TeV", *JHEP* **10** (2011) 132, doi:10.1007/JHEP10(2011)132, arXiv:1107.4789.

[77] CMS Collaboration, "Performance of photon reconstruction and identification with the CMS detector in proton-proton collisions at $\sqrt{s} = 8$ TeV", *JINST* **10** (2015) P08010, doi:10.1088/1748-0221/10/08/P08010, arXiv:1502.02702.

[78] T. Junk, "Confidence level computation for combining searches with small statistics", *Nucl. Instrum. Meth. A* **434** (1999) 435, doi:10.1016/S0168-9002(99)00498-2, arXiv:hep-ex/9902006.

[79] A. L. Read, "Presentation of search results: the CL_s technique", *J. Phys. G* **28** (2002) 2693, doi:10.1088/0954-3899/28/10/313.

[80] G. Cowan, K. Cranmer, E. Gross, and O. Vitells, "Asymptotic formulae for likelihood-based tests of new physics", *Eur. Phys. J. C* **71** (2011) 1554, doi:10.1140/epjc/s10052-011-1554-0, arXiv:1007.1727. [Erratum: doi:10.1140/epjc/s10052-013-2501-z].

[81] ATLAS and CMS Collaboration, "Procedure for the LHC Higgs boson search combination in Summer 2011", technical report, CERN, Aug, 2011.

[82] E. Gross and O. Vitells, "Trial factors for the look elsewhere effect in high energy physics", *Eur. Phys. J. C* **70** (2010) 525, doi:10.1140/epjc/s10052-010-1470-8, arXiv:1005.1891.

[83] CMS Collaboration, "Searches for additional Higgs bosons and vector leptoquarks in $\tau\tau$ final states in proton-proton collisions at $\sqrt{s} = 13$ TeV", CMS Physics Analysis Summary CMS-PAS-HIG-21-001, CERN, 2022.

[84] CMS Collaboration, "Search for high mass resonances decaying into W^+W^- in the dileptonic final state with 138 fb^{-1} of proton-proton collisions at $\sqrt{s} = 13$ TeV", CMS Physics Analysis Summary CMS-PAS-HIG-20-016, CERN, 2022.

[85] CMS Collaboration, "Search for a standard model-like Higgs boson in the mass range between 70 and 110 GeV in the diphoton final state in proton-proton collisions at $\sqrt{s} = 8$ and 13 TeV", *Phys. Lett. B* **793** (2019) 320, doi:10.1016/j.physletb.2019.03.064, arXiv:1811.08459.

[86] CMS Collaboration, "Combination of searches for Higgs boson pair production in proton-proton collisions at $\sqrt{s} = 13$ TeV", *Phys. Rev. Lett.* **122** (2019) 121803, doi:10.1103/PhysRevLett.122.121803, arXiv:1811.09689.